VIP All-Solid-State Batteries Very Important Paper

How to cite: *Angew. Chem. Int. Ed.* **2022,** *61,* e202203484
International Edition: doi.org/10.1002/anie.202203484
German Edition: doi.org/10.1002/ange.202203484

Methylamine Lithium Borohydride as Electrolyte for All-Solid-State Batteries

*Jakob B. Grinderslev, Lasse N. Skov, Jacob G. Andreasen, Shaiq Ghorwal, Jørgen Skibsted, and Torben R. Jensen**

Abstract: Fast Li-ion conductivity at room temperature is a major challenge for utilization of all-solid-state Li batteries. Metal borohydrides with neutral ligands are a new emerging class of solid-state ionic conductors, and here we report the discovery of a new mono-methylamine lithium borohydride with very fast Li^+ conductivity at room temperature. $LiBH_4{\cdot}CH_3NH_2$ crystallizes in the monoclinic space group $P2_1/c$, forming a two-dimensional unique layered structure. The layers are separated by hydrophobic $-CH_3$ moieties, and contain large voids, allowing for fast Li-ionic conduction in the interlayers, $\sigma(Li^+) = 1.24 \times 10^{-3}\,S\,cm^{-1}$ at room temperature. The electronic conductivity is negligible, and the electrochemical stability is ≈ 2.1 V vs Li. The first all-solid-state battery using a lithium borohydride with a neutral ligand as the electrolyte, Li-metal as the anode and TiS_2 as the cathode is demonstrated.

Introduction

Lithium-ion batteries have successfully been commercialized for small portable electronic devices and more recently for electric cars and large-scale energy storage. However, the organic liquid electrolytes used in commercial applications cause safety concerns and are incompatible with lithium metal anodes, which significantly reduces the relative energy density by using graphite anodes.[1] Solid-state batteries, using inorganic solid electrolytes, may offer higher energy and power density, besides other benefits such as longer cycle life, less polarization, increased safety, and higher thermal and electrochemical stability.[1–4] Furthermore, the mechanical rigidity of the solid electrolyte may prevent lithium dendrite formation, allowing for the use of lithium-metal anodes.[1–3]

Solid electrolytes often display low ionic conductivity and sluggish kinetics at interfaces, but several promising candidates have been discovered in the recent years, with developments mainly concerned with oxides and chalcogenides.[5] Oxide-based materials often show high electrochemical stability, but suffer from high grain boundary resistance and poor compatibility with Li-metal.[3,6] On the other hand, chalcogenide-based materials are more ductile and often show lower grain-boundary resistance and higher ionic conductivity, but suffer from a lower electrochemical stability.[3,6,7]

Complex metal hydrides have emerged as a new class of superionic solid-state conductors and may offer several advantages in terms of higher gravimetric energy densities, apparent compatibility with metal anodes due to their reducing nature, and better interfacial contact and easier manufacturing as a result of high deformability.[7–13] The interest in complex metal hydrides was initiated by the discovery of high Li^+ conductivity in the high-temperature polymorph of $LiBH_4$ above $\approx 117\,^\circ C$.[14] Despite significant efforts to increase the Li^+ conductivity of $LiBH_4$-based materials at lower temperatures, e.g. using a variety of additives, nano-confinement, anion substitution or by partial dehydrogenation,[15–24] there are only few reports of sufficiently high Li^+ conductivity at ambient conditions, i.e. $\sigma(Li^+) > 10^{-3}\,S\,cm^{-1}$. Recently, it has been demonstrated that neutral ligands can significantly increase the conductivity of metal borohydrides, observed for $LiBH_4$ coordinated with NH_3 or NH_3BH_3, but also applicable to multivalent ionic conductors as reported for $Mg(BH_4)_2$ with NH_3, NH_3BH_3 or $NH_2CH_3CH_3NH_2$.[15,25–30] The fast cation mobility is suggested to result from the flexible structure owing to an extended network of dihydrogen bonds, a relatively free exchange of the neutral ligand and a flexible coordination of the BH_4^- group, or due to a distortion of the nearest coordination sphere of the cation.[15,27–30]

Here we investigate the effects of a neutral molecule also containing a hydrophobic moiety and report the first member in a new class of borohydride compounds - methylamine metal borohydrides. We report the synthesis and crystal structure of methylamine lithium borohydride, $LiBH_4{\cdot}CH_3NH_2$, which display an extremely high Li^+ conductivity at room temperature, making it a promising solid-state electrolyte. The compound is characterized by powder X-ray diffraction (PXD), ^{11}B magic-angle spinning nuclear magnetic resonance (^{11}B MAS NMR) spectroscopy,

[*] Dr. J. B. Grinderslev, L. N. Skov, J. G. Andreasen, S. Ghorwal, Prof. J. Skibsted, Prof. T. R. Jensen
Interdisciplinary Nanoscience Center (iNANO) and Department of Chemistry, Aarhus University
Langelandsgade 140, 8000 Aarhus C (Denmark)
E-mail: trj@chem.au.dk

Fourier transformed infrared spectroscopy (FTIR) and thermal analysis, and the electrochemical properties are assessed using electrochemical impedance spectroscopy (EIS), cyclic voltammetry (CV) and galvanostatic cycling (GC). A full solid-state battery is also assembled using a Li-metal anode and a layered TiS_2 cathode.

Results and Discussion

$LiBH_4{\cdot}CH_3NH_2$ is prepared in a gas-solid reaction between $LiBH_4$ and CH_3NH_2, after which excess CH_3NH_2 is removed by evacuation in vacuum. FTIR revealed new absorption modes, which has been assigned according to related compounds from literature, see Figure S1a.[31–33] $LiBH_4{\cdot}CH_3NH_2$ show similar B–H stretching (2000–2500 cm^{-1}) and bending (1000–1400 cm^{-1}) modes as observed for $LiBH_4$.[31] New modes assigned to CH_3NH_2 are observed as N–H stretching (3300 and 3350 cm^{-1}), C–H stretching (2750–3000 cm^{-1}), N–H bending (1460 and 1600 cm^{-1}) modes, and a region from 850–1350 cm^{-1} containing B–H bending, C–H bending, CH_3 rocking and C–N stretching modes. Weak NH_2 wagging modes are observed at 680–760 cm^{-1}, significantly less intense compared to molecular CH_3NH_2,[32] most likely as a result of restrained movement from the coordination to Li^+ in the crystal structure. $LiBH_4{\cdot}CH_3NH_2$ is hygroscopic and slowly react with water in contact with air, and all vibrational modes corresponding to BH_4^- and CH_3NH_2 have disappeared after 24 h (Figure S1b).

Crystal Structure of $LiBH_4{\cdot}CH_3NH_2$

SR PXD data revealed that all Bragg reflections corresponding to $LiBH_4$ had disappeared and the observed Bragg reflections could be indexed in a monoclinic unit cell with space group symmetry $P2_1/c$ and unit cell parameters $a=9.1972(2)$, $b=7.2148(1)$, $c=7.1157(1)$ Å, $\beta=96.4930(5)°$ and $V=469.14(2)$ Å^3 at $T=-23$ °C, suggesting the composition $LiBH_4{\cdot}CH_3NH_2$ with $Z=4$. The structure was solved ab initio and the final Rietveld refinement is shown in Figure S2, providing a convincing fit to the observed SR PXD data.[57]

In the structure of $LiBH_4{\cdot}CH_3NH_2$ (Figure 1a), one unique Li position is coordinated by three BH_4^- and one CH_3NH_2, forming $[Li(CH_3NH_2)(BH_4)_3]$ tetrahedral units (Figure 1b). The BH_4^- anion coordinates to two Li via edge-sharing (κ^2) and one with a distorted face-sharing (κ^3), resulting in the coordination number 8 for Li. The $[Li(CH_3NH_2)(BH_4)_3]$ tetrahedral units are connected by edge- or corner-sharing via bridging BH_4^- groups, forming two-dimensional layers in the *bc*-plane (Figure 1c), which are stacked along the *a*-axis. The layers are interconnected by hydrophobic interactions between the $-CH_3$ groups. The Li–N distance is 2.05 Å and the Li–B distances are in the range 2.49–2.67 Å, similar to what is observed for $LiBH_4{\cdot}NH_3$.[34] However, the structural morphology is different from $LiBH_4{\cdot}NH_3$, which forms one-dimensional chains.

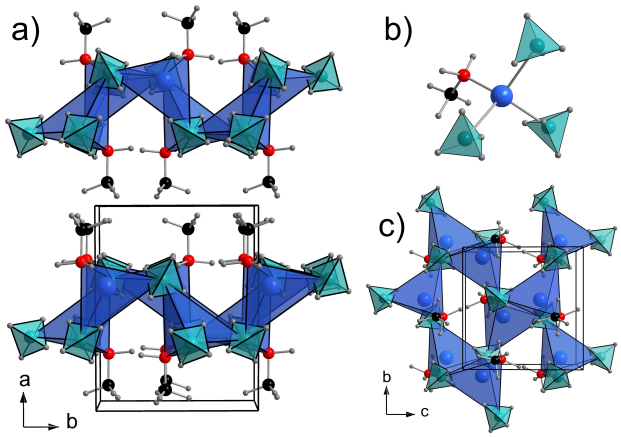

Figure 1. The crystal structure of $LiBH_4{\cdot}CH_3NH_2$. a) The layers viewed from the *ab*-plane, b) the local lithium coordination and c) a layer viewed in the *bc*-plane. Color scheme: Li^+ (blue), BH_4^- (light blue tetrahedra), N (red), C (black) and H (grey).

Analysis of voids in the crystal structure reveals large cavities along the *c*-axis, forming a preferred one-dimensional pathway large enough to accommodate an interstitial migrating Li^+ ion. These cavities are connected along the *b*-axis cell edges, resulting in a two-dimensional conduction pathway (Figure S3). The preferred one-dimensional conduction pathway is shown in Figure 2, where the conduction path for an interstitial Li^+ ion is a zig-zag pattern following the positions of the BH_4^- groups. The BH_4^- groups can likely reorient to stabilize the coordination of both the framework and migrating interstitial Li^+, while CH_3NH_2 may be exchanged between the two Li^+ ions, similar to the conduction mechanism reported for the analogous compounds, $LiBH_4{\cdot}^1/_2NH_3$ and $Mg(BH_4)_2{\cdot}NH_3$.[15,27]

The ^{11}B ($I=3/2$) MAS NMR spectrum of the central ($m=^1/_2 \leftrightarrow m=-^1/_2$) and satellite ($m=\pm^1/_2 \leftrightarrow m=\pm^3/_2$) transitions for $LiBH_4{\cdot}CH_3NH_2$ (Figure 3a) shows a centerband and manifold of spinning sidebands (ssbs) from a unique

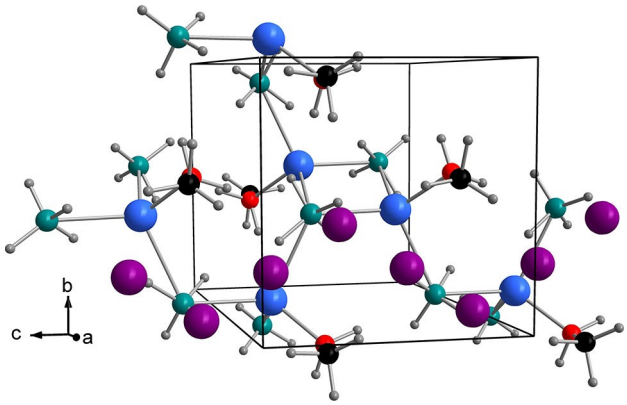

Figure 2. The preferred one-dimensional conduction pathway along the *c*-axis in $LiBH_4{\cdot}CH_3NH_2$. Color scheme: Interstitial Li^+ (purple), framework Li^+ (blue), BH_4^- (light blue tetrahedra), N (red), C (black) and H (grey).

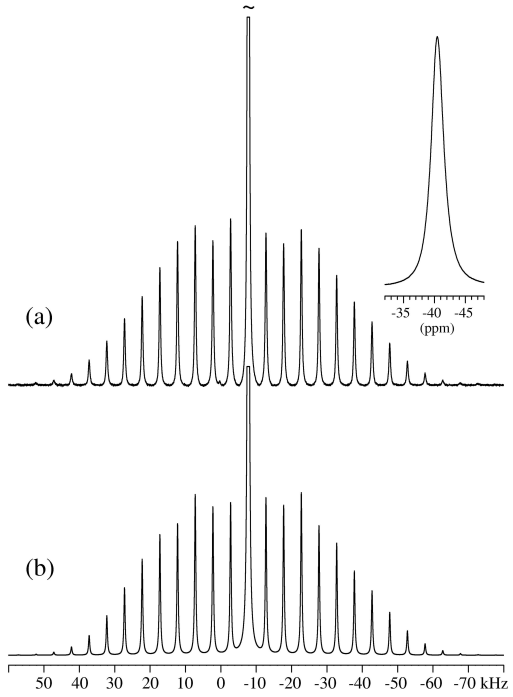

Figure 3. a) ^{11}B MAS NMR spectrum of the central and satellite transitions for $LiBH_4{\cdot}CH_3NH_2$ acquired at 14.09 T using a spinning speed of $\nu_R = 5.0$ kHz, and a sample temperature of 12.0 °C. The inset illustrates the centerband resonance. b) Optimized simulation of the spectrum in (a), corresponding to the ^{11}B interaction parameters given in the text.

boron-site in $LiBH_4{\cdot}CH_3NH_2$, in accordance with the crystal structure. Moreover, the ^{11}B isotropic chemical shift, $\delta_{iso} = -40.5$ ppm, reveals the presence of a BH_4^- unit, which is clearly different from the corresponding borohydride unit in *o*-$LiBH_4$, $\delta_{iso} = -41.0$ ppm,[37] as revealed from a spectrum acquired under the same experimental conditions (Figure S4) and in agreement with a previous ^{11}B NMR study.[38] The manifold of ssbs can be simulated by considering the mutual presence of the quadrupole coupling interaction and the chemical shift anisotropy (CSA), using the approach described in refs.[39,40] Least-squares fitting of simulated to experimental ssb intensities gives the optimized simulation shown in Figure 3b, corresponding to the quadrupole coupling parameters, $C_Q = 98 \pm 8$ kHz and $\eta_Q = 0.42 \pm 0.03$, the CSA parameters, $\delta_{iso} = -40.5 \pm 0.1$ ppm, $\delta_\sigma = 17 \pm 4$ ppm and $\eta_\sigma = 0.56 \pm 0.30$, and the relative orientation of the two tensorial interactions defined by the Euler angles $\psi = 180°$, $\chi = 37° \pm 25°$ and $\xi = 0°$ at a temperature of 12.0 °C (definition of the interaction parameters are given in refs. [39,40]). These parameters are very similar to the corresponding values reported for *o*-$LiBH_4$ at 25 °C ($\delta_{iso} = -41.0$ ppm, $C_Q = 99$ kHz, $\eta_Q = 0.91$, $\delta_\sigma = 30$ ppm, $\eta_\sigma = 0.91$),[38] suggesting that the local geometry or dynamics of the BH_4^- units in $LiBH_4{\cdot}CH_3NH_2$ and *o*-$LiBH_4$ are similar. A $^{13}C\{^1H\}$ MAS NMR spectrum of $LiBH_4{\cdot}CH_3NH_2$ has also been acquired (Figure S5), which shows a single resonance at 28.5 ppm, in good agreement with the ^{13}C chemical shift of CH_3NH_2 in the liquid state.

Thermal Analysis

Figure 4a and b show the in situ SR PXD and TG-DSC-MS data of $LiBH_4{\cdot}CH_3NH_2$ during heating. All Bragg reflections correspond to $LiBH_4{\cdot}CH_3NH_2$ and disappear at 45 to 50 °C, after which the sample becomes amorphous. No changes are observed during cooling. An endothermic event at 44 °C along with visual inspection (Figure S6) suggests that the sample melts and marks the onset of a gradual release of CH_3NH_2 and a minor amount of H_2. A second endothermic event at 105 °C coincides with an increased release of CH_3NH_2 and may be related to the orthorhombic to hexagonal polymorphic transition of $LiBH_4$.[41] A total mass loss of 55.7 wt % is observed upon heating to 120 °C, which agree well with the expected mass of one molecule of CH_3NH_2 per formula unit (58.8 wt %, calc.).

Electrochemical characterization

The Li^+ conductivity was assessed using EIS measurements of a symmetric cell with Mo-blocking electrodes, Mo|$LiBH_4{\cdot}CH_3NH_2$|Mo (Figure 4c, d). The cell resistance decreased rapidly as a function of time at room temperature (Figure 4c), resulting in an increase of the conductivity from $\sigma(Li^+) = 2.73 \times 10^{-5}$ S cm^{-1} to 1.24×10^{-3} S cm^{-1} in 10 hours, i.e. an increase of almost two orders of magnitude. This could indicate a decrease in the interface resistance in the grain boundaries within the pellet or towards the Mo-electrodes. To ensure that this effect is not a reaction with air, a measurement was also conducted in the glovebox, also showing a decreasing resistance as a function of time. The cell resistance stabilized after 10 hours, after which the temperature-dependent Li^+ conductivity were measured in the low-temperature range $T = -18$ to 29 °C to avoid any decomposition of the sample. The Li^+ conductivity of $LiBH_4{\cdot}CH_3NH_2$ is the highest of all known $LiBH_4$ derivatives, and the conductivity is more than five orders of magnitude higher than pristine $LiBH_4$ at room temperature (Figure 4d). More importantly, the Li^+ conductivity is sufficiently high for battery operation at ambient conditions, $\sigma(Li^+) > 10^{-4}$ S cm^{-1}.[3] The activation energy for Li^+ conduction is similar to several other $LiBH_4$ derivatives with a value of $E_a = 0.83$ eV for the temperature range $T = -6$ to 29 °C (Figure S7), while the conductivity at $T = -18$ °C appear to be slightly lower than expected from a linear Arrhenius behavior.

A DC voltage polarization of a symmetric cell with blocking electrodes was used to validate that the high conductivity was not electronic. The peak current (i_T) to a 0.5 V polarization resulted in a current response of 4.18×10^{-5} μA cm^{-1} and a steady state current (i_e) of 1.36×10^{-8} μA cm^{-1} (Figure S8). From the relation $t_{ion} = i_{ion}/i_T = (i_T - i_e)/i_T$, the ionic transport number (t_{ion}) was estimated to 0.9983. The low electronic conductivity is an important property to suppress dendrite formation, and a similar low value was found for pure $LiBH_4$.[35,42,43]

The electrochemical stability of $LiBH_4{\cdot}CH_3NH_2$ was investigated with CV in a two-electrode setup with Mo as

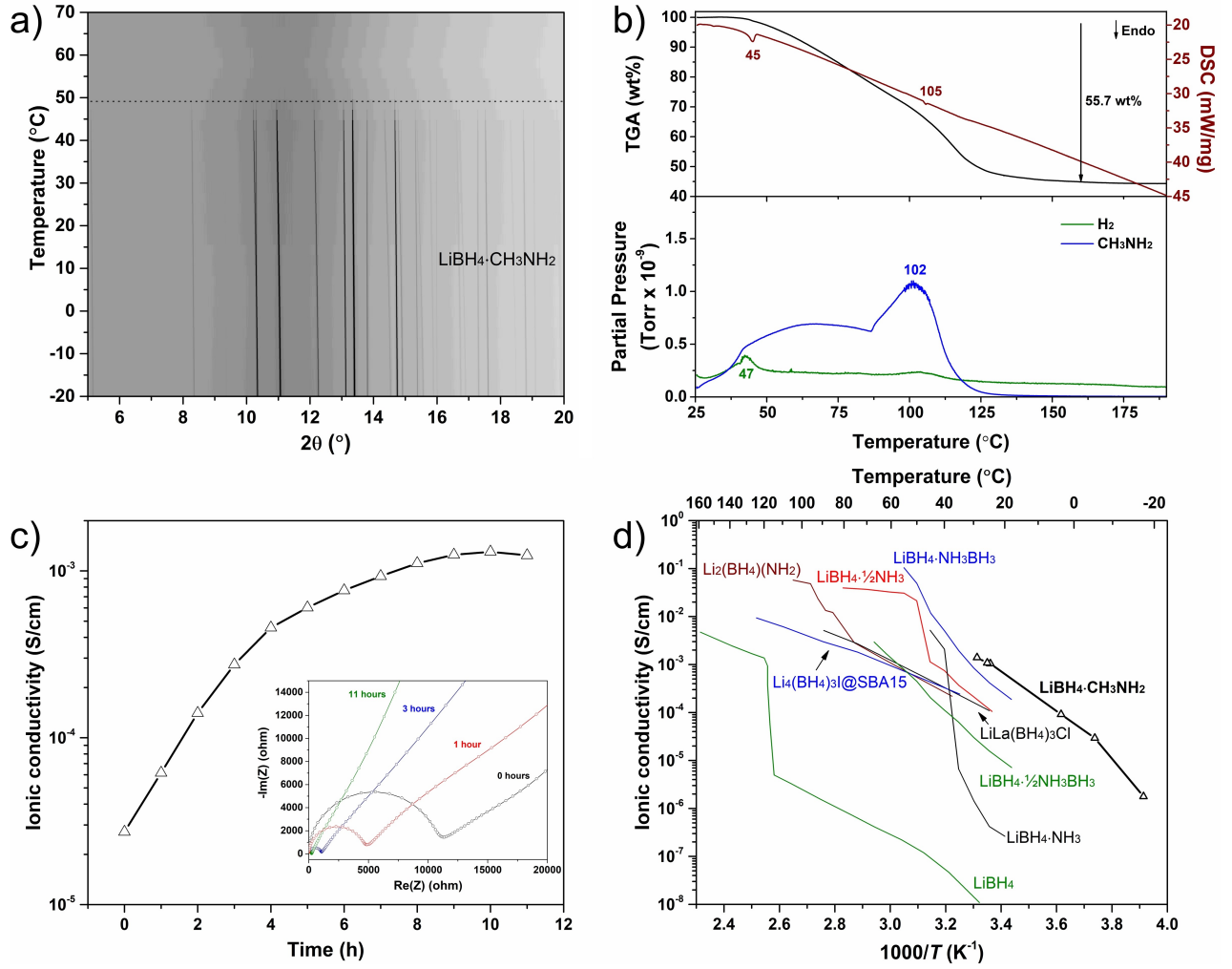

Figure 4. a) In situ SR PXD data (λ = 0.824958 Å, 5 °C/min) and b) TG-DSC-MS data (0.5 °C min^{-1}) of $LiBH_4{\cdot}CH_3NH_2$. c) time-dependence of the Li^+ conductivity at $T = 24$ °C and selected Nyquist plots (inset) and d) temperature-dependence of the Li^+ conductivity compared to other selected $LiBH_4$ derivatives.[14,15,21,25,26,35,36]

the working electrode and Li as both the counter and reference electrode (Figure 5a). At low potentials, Li plating/stripping on the Mo electrode is observed below and above 0 V, respectively, with an increase in current as a function of cycle number. This indicates an improved contact or interface between the electrolyte and Li-metal during cycling. An anodic current starts to flow at 2.1 V, corresponding to the oxidation of the BH_4^- anion as predicted previously from DFT calculations and in agreement with that of other $LiBH_4$-based electrolytes.[44–46] In addition, a small oxidative current flows at 1.2 V, which may be the cause of the current fluctuations (spikes) observed at higher cycle numbers, e.g. cycle 10.

An all-solid-state battery with $LiBH_4{\cdot}CH_3NH_2$ as the solid-state electrolyte and TiS_2 as the cathode was assembled and tested with CV (Figure S9) and GC (Figure 5b). TiS_2 was chosen as the cathode material, as it has a potential ($\approx$2 V) within the electrochemical stability of $LiBH_4{\cdot}CH_3NH_2$, and because it is a well-studied cathode for Li-batteries.[47] As indicated by the voltammogram in Figure S9, the lithiation and dilithiation in TiS_2 are observed (Figure S9 insert), but an irreversible anodic current with a much higher current than the dilithiation of TiS_2 starts at 2.1 V. During galvanostatic cycling of the same cell with a C-rate of C/20, similar events are present in the charge/discharge curves, i.e. an oxidation occurs at 2.2 V until the charging step is cut-off after 30 hours. The maximum discharge capacity (2nd discharge) resulted in a capacity of 69 mAh g^{-1}, which is $\approx$30 % of the theoretical capacity assuming one Li per TiS_2. These results indicate a side-reaction at the interface between TiS_2 and the $LiBH_4{\cdot}CH_3NH_2$ electrolyte, due to the limited oxidative stability of the BH_4^- anion (<2.1 V). For comparison, there are reports of more stable cycling in solid-state batteries of $Li|LiBH_4|TiS_2$, where a stable $Li_2B_{12}H_{12}$-containing solid-electrolyte interface is suggested to form.[48] This is observed as a low initial discharge capacity due to self-discharge from the formation of the interface layer, while a higher discharge capacity and more stable cycling is observed subsequently.[48] Thus, this suggests that a different and unfavorable interface

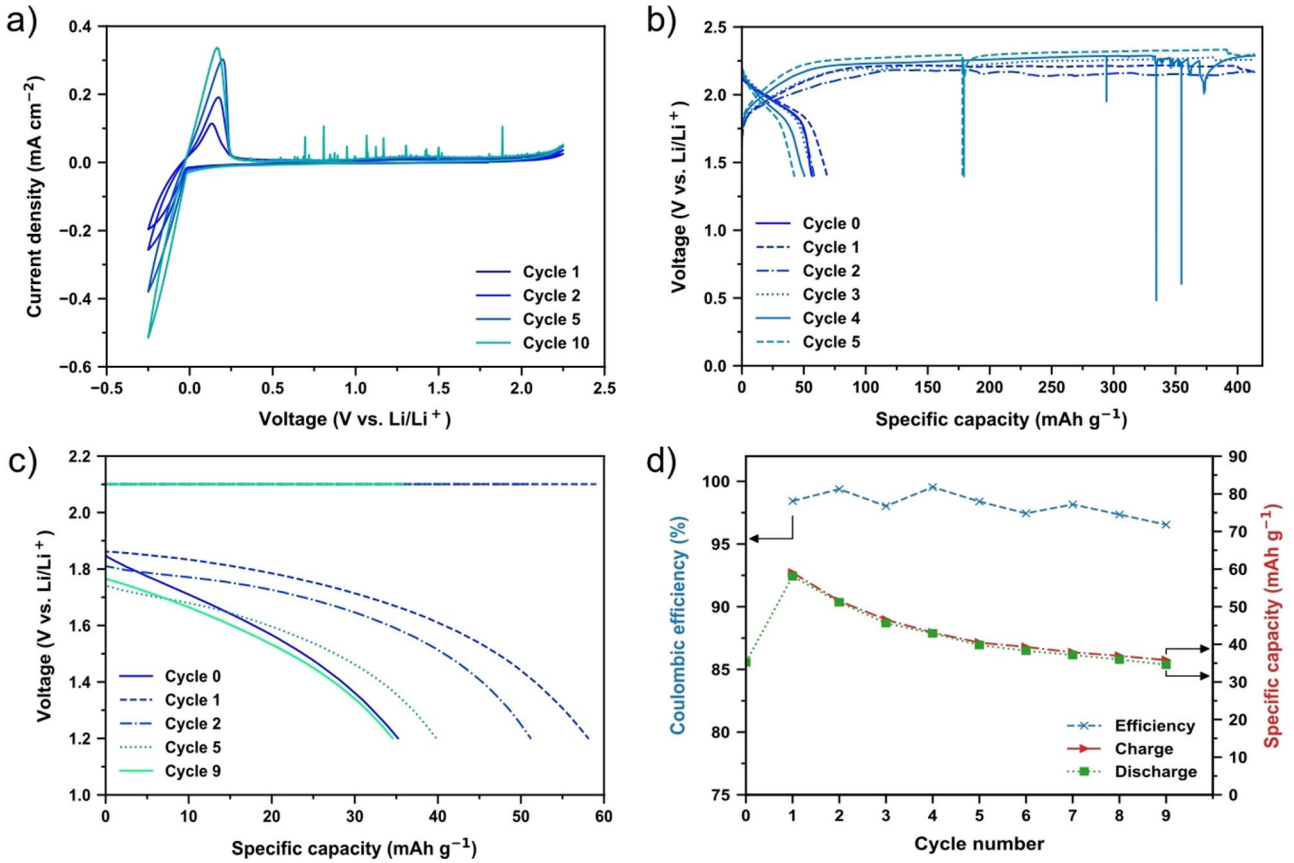

Figure 5. a) Cyclic voltammogram of an asymmetric Li | $LiBH_4{\cdot}CH_3NH_2$ | Mo cell at room temperature with a scan rate of 1.0 mV s^{-1} in the potential range −0.25 V to 2.25 V. b) Galvanostatic cycling at C/20 (46 μA cm^{-2}) of an all-solid-state Li | $LiBH_4{\cdot}CH_3NH_2$ | TiS_2 cell (cathode composition: TiS_2: $LiBH_4{\cdot}CH_3NH_2$ = 0.65 : 0.35 wt%) with a voltage cutoff of 1.4 V (and 2.4 V) and a time cutoff of 30 h. c) An all-solid-state Li | $LiBH_4{\cdot}CH_3NH_2$ | TiS_2 cell (cathode composition: TiS_2:$LiBH_4{\cdot}CH_3NH_2$ = 0.78 : 0.22 wt%) charged with constant current/constant voltage charge at 2.1 V with a limiting current of 10 μA and constant current discharge at C/20 (110 μA cm^{-2}) with a voltage cutoff at 1.2 V. d) The charge (red) / discharge (green) capacity and coulombic efficiency as a function of cycles for the battery shown in c). All electrochemical characterization was performed at T = 30 °C.

is formed for the $LiBH_4{\cdot}CH_3NH_2$ electrolyte, which cannot protect the electrolyte towards further oxidation.

In an attempt to avoid this side-reaction, an additional cell employing constant voltage charging at 2.1 V with a cut-off current of 10 μA and constant-current discharging at C/20 was investigated (Figure 5c). The cell had a larger separator, which gives rise to a higher overpotential, and a higher TiS_2 mass loading. However, the performance of this cell resulted in a higher coulombic efficiency (≈98 %), but with similar capacities (Figure 5d), indicating that the side-reaction can be reduced by tuning the cycling procedure.

In high voltage battery applications, the use of $LiBH_4{\cdot}CH_3NH_2$ as an electrolyte thus depend on the formation of a more favorable interface to lower the voltage gradient across the electrolyte. Nanoconfined $LiBH_4$, and derivatives thereof, have previously shown to exhibit an increased stability of a cell due to the formation of a favorable interface.[20,42,49] Such an interface requires a very low electronic conductivity to minimize the degradation of the electrolyte.[50] Alternatively, the electrolyte can be used in combination with a catholyte, i.e. an electrolyte stable towards the cathode material, or by coating the cathode material. These approaches are already under investigation for the thiophosphate- and argyrodite-based Li-electrolytes, which also suffer from relatively low oxidative stabilities.[51–56]

Conclusion

In summary, we report the new compound methylamine lithium borohydride, $LiBH_4{\cdot}CH_3NH_2$, which exhibits the highest reported room temperature Li-ion conductivity observed for a $LiBH_4$-based material, $\sigma(Li^+) = 1.24 \times 10^{-3}$ S cm^{-1} at 24 °C. Introducing the neutral ligand CH_3NH_2 creates a two-dimensional monoclinic structure. The structure is built from layers in the *bc*-plane, consisting of $[Li(CH_3NH_2)(BH_4)_3]$ tetrahedral units that are connected by bridging borohydride groups. The structure contains voids in the interlayers that create a preferred one-dimensional Li-ion conduction channel along the *c*-axis, which is connected into a two-dimensional conduction network via voids along the *b*-axis. Electrochemical characterization revealed an oxidative stability of ≈2.1 V vs. Li and reversible plating/stripping on a Mo-electrode, similar to other $LiBH_4$-based materials. The first proof-of-concept battery for $LiBH_4$ with

a neutral ligand was demonstrated with a TiS_2 cathode, reaching a maximum discharge capacity of 69 $mAh\,g^{-1}$ at 30 °C. The oxidative degradation of the electrolyte (> 2.1 V) was suppressed by constant current/constant voltage charging at 2.1 V, resulting in a coulombic efficiency of ≈98 %.

This work demonstrates a new fast Li^+-conducting electrolyte that may allow for all-solid-state Li-batteries to be operated at ambient conditions. Further efforts to stabilize the high conductivity to even lower temperatures may be achieved by mixing with nanoparticles as previously reported, e.g. with MgO and Al_2O_3,[17,18,20,28] and further screening for compatible cathode or catholyte materials may result in new types of energy-dense all-solid-state lithium batteries.

Acknowledgements

The work was supported by the Danish Council for Independent Research, Nature and Universe (Danscatt), and Technology and Production (SOS-MagBat DFF9041-00226B and CaMBat DFF-0217-00327B). Affiliation with the Center for Integrated Materials Research (iMAT) at Aarhus University is gratefully acknowledged. We also thank beamline I11 at the Diamond Light Source for provision of beamtime and the local contacts Stephen Thompson and Sarah Day for assistance with data collection.

Conflict of Interest

The authors declare no conflict of interest.

Data Availability Statement

The data that support the findings of this study are available in the Supporting Information of this article.

Keywords: Complex Hydrides · Energy Storage · Li-Metal Batteries · Solid-State Batteries · Solid-State Electrolytes

[1] J. Janek, W. G. Zeier, *Nat. Energy* **2016**, *1*, 16141.
[2] P. Knauth, *Solid State Ionics* **2009**, *180*, 911–916.
[3] Z. Zhang, Y. Shao, B. Lotsch, Y.-S. Hu, H. Li, J. Janek, L. F. Nazar, C.-W. Nan, J. Maier, M. Armand, L. Chen, *Energy Environ. Sci.* **2018**, *11*, 1945–1976.
[4] J. Wang, G. Huang, X.-B. Zhang, *Batteries Supercaps* **2020**, *3*, 1006–1015.
[5] Y. Pang, J. Pan, J. Yang, S. Zheng, C. Wang, *Electrochem. Energy Rev.* **2021**, *4*, 169–193.
[6] K. H. Park, Q. Bai, D. H. Kim, D. Y. Oh, Y. Zhu, Y. Mo, Y. S. Jung, *Adv. Energy Mater.* **2018**, *8*, 1800035.
[7] R. Mohtadi, *Molecules* **2020**, *25*, 1791.
[8] M. Paskevicius, L. H. Jepsen, P. Schouwink, R. Černý, D. B. Ravnsbæk, Y. Filinchuk, M. Dornheim, F. Besenbacher, T. R. Jensen, *Chem. Soc. Rev.* **2017**, *46*, 1565–1634.
[9] K. T. Møller, D. Sheppard, D. B. Ravnsbæk, C. E. Buckley, E. Akiba, H.-W. Li, T. R. Jensen, *Energies* **2017**, *10*, 1645.
[10] A. Unemoto, M. Matsuo, S. Orimo, *Adv. Funct. Mater.* **2014**, *24*, 2267–2279.
[11] L. Duchêne, A. Remhof, H. Hagemann, C. Battaglia, *Energy Storage Mater.* **2020**, *25*, 782–794.
[12] J. B. Grinderslev, M. B. Amdisen, L. N. Skov, K. T. Møller, L. G. Kristensen, M. Polanski, M. Heere, T. R. Jensen, *J. Alloys Compd.* **2022**, *896*, 163014.
[13] Y. Pang, Y. Liu, J. Yang, S. Zheng, C. Wang, *Mater. Today Nano* **2022**, *18*, 100194.
[14] M. Matsuo, Y. Nakamori, S. Orimo, H. Maekawa, H. Takamura, *Appl. Phys. Lett.* **2007**, *91*, 224103.
[15] Y. Yan, J. B. Grinderslev, Y.-S. Lee, M. Jørgensen, Y. W. Cho, R. Černý, T. R. Jensen, *Chem. Commun.* **2020**, *56*, 3971–3974.
[16] Suwarno, P. Ngene, A. Nale, T. M. Eggenhuisen, M. Oschatz, J. P. Embs, A. Remhof, P. E. de Jongh, *J. Phys. Chem. C* **2017**, *121*, 4197–4205.
[17] V. Gulino, L. Barberis, P. Ngene, M. Baricco, P. E. de Jongh, *ACS Appl. Energy Mater.* **2020**, *3*, 4941–4948.
[18] L. M. de Kort, J. Harmel, P. E. de Jongh, P. Ngene, *J. Mater. Chem. A* **2020**, *8*, 20687–20697.
[19] H. Maekawa, M. Matsuo, H. Takamura, M. Ando, Y. Noda, T. Karahashi, S. Orimo, *J. Am. Chem. Soc.* **2009**, *131*, 894–895.
[20] R. Zhang, W. Zhao, Z. Liu, S. Wei, Y. Yan, Y. Chen, *Chem. Commun.* **2021**, *57*, 2380–2383.
[21] M. Matsuo, A. Remhof, P. Martelli, R. Caputo, M. Ernst, Y. Miura, T. Sato, H. Oguchi, H. Maekawa, H. Takamura, A. Borgschulte, A. Züttel, S. Orimo, *J. Am. Chem. Soc.* **2009**, *131*, 16389–16391.
[22] M. Zhu, Y. Pang, F. Lu, X. Shi, J. Yang, S. Zheng, *ACS Appl. Mater. Interfaces* **2019**, *11*, 14136–14141.
[23] F. Cuevas, M. B. Amdisen, M. Baricco, C. E. Buckley, Y. W. Cho, P. de Jongh, L. M. de Kort, J. B. Grinderslev, V. Gulino, B. C. Hauback, M. Heere, T. Humphries, T. R. Jensen, S. Kim, K. Kisu, Y.-S. Lee, H.-W. Li, R. Mohtadi, K. T. Møller, P. Ngene, D. Noréus, S. Orimo, M. Paskevicius, M. Polanski, S. Sartori, L. N. Skov, M. H. Sørby, B. C. Wood, V. A. Yartys, M. Zhu, M. Latroche, *Prog. Energy* **2022**, *4*, 032001.
[24] L. M. de Kort, V. Gulino, P. E. de Jongh, P. Ngene, *J. Alloys Compd.* **2022**, *901*, 163474.
[25] T. Zhang, Y. Wang, T. Song, H. Miyaoka, K. Shinzato, H. Miyaoka, T. Ichikawa, S. Shi, X. Zhang, S. Isobe, N. Hashimoto, Y. Kojima, *Joule* **2018**, *2*, 1522–1533.
[26] H. Liu, Z. Ren, X. Zhang, J. Hu, M. Gao, H. Pan, Y. Liu, *Chem. Mater.* **2020**, *32*, 671–678.
[27] Y. Yan, W. Dononelli, M. Jørgensen, J. B. Grinderslev, Y.-S. Lee, Y. W. Cho, R. Černý, B. Hammer, T. R. Jensen, *Phys. Chem. Chem. Phys.* **2020**, *22*, 9204–9209.
[28] Y. Yan, J. B. Grinderslev, M. Jørgensen, L. N. Skov, J. Skibsted, T. R. Jensen, *ACS Appl. Energy Mater.* **2020**, *3*, 9264–9270.
[29] K. Kisu, S. Kim, M. Inukai, H. Oguchi, S. Takagi, S. Orimo, *ACS Appl. Energy Mater.* **2020**, *3*, 3174–3179.
[30] E. Roedern, R.-S. Kühnel, A. Remhof, C. Battaglia, *Sci. Rep.* **2017**, *7*, 46189.
[31] V. D'Anna, A. Spyratou, M. Sharma, H. Hagemann, *Spectrochim. Acta Part A* **2014**, *128*, 902–906.
[32] J. R. Durig, C. Zheng, *Struct. Chem.* **2001**, *12*, 137–148.
[33] J. B. Grinderslev, M. B. Ley, Y.-S. Lee, L. H. Jepsen, M. Jørgensen, Y. W. Cho, J. Skibsted, T. R. Jensen, *Inorg. Chem.* **2020**, *59*, 7768–7778.
[34] S. R. Johnson, W. I. F. David, D. M. Royse, M. Sommariva, C. Y. Tang, F. P. A. Fabbiani, M. O. Jones, P. P. Edwards, *Chem. Asian J.* **2009**, *4*, 849–854.
[35] F. Lu, Y. Pang, M. Zhu, F. Han, J. Yang, F. Fang, D. Sun, S. Zheng, C. Wang, *Adv. Funct. Mater.* **2019**, *29*, 1809219.

[36] M. B. Ley, S. Boulineau, R. Janot, Y. Filinchuk, T. R. Jensen, *J. Phys. Chem. C* **2012**, *116*, 21267–21276.
[37] J. Skibsted, S. Payandeh, M. B. Ley, T. R. Jensen, *J. Phys. Chem. C* **2021**, *125*, 1113–1124.
[38] L. M. Arnbjerg, D. B. Ravnsbæk, Y. Filinchuk, R. T. Vang, Y. Cerenius, F. Besenbacher, J.-E. Jørgensen, H. J. Jakobsen, T. R. Jensen, *Chem. Mater.* **2009**, *21*, 5772–5782.
[39] J. Skibsted, N. C. Nielsen, H. Bildsøe, H. J. Jakobsen, *Chem. Phys. Lett.* **1992**, *188*, 405–412.
[40] J. Skibsted, N. C. Nielsen, H. Bildsøe, H. J. Jakobsen, *J. Am. Chem. Soc.* **1993**, *115*, 7351–7362.
[41] A. Züttel, S. Rentsch, P. Fischer, P. Wenger, P. Sudan, Ph. Mauron, Ch. Emmenegger, *J. Alloys Compd.* **2003**, *356–357*, 515–520.
[42] S. Das, P. Ngene, P. Norby, T. Vegge, P. E. D. Jongh, D. Blanchard, *J. Electrochem. Soc.* **2016**, *163*, A2029–A2034.
[43] F. Han, A. S. Westover, J. Yue, X. Fan, F. Wang, M. Chi, D. N. Leonard, N. J. Dudney, H. Wang, C. Wang, *Nat. Energy* **2019**, *4*, 187–196.
[44] W. D. Richards, L. J. Miara, Y. Wang, J. C. Kim, G. Ceder, *Chem. Mater.* **2016**, *28*, 266–273.
[45] Z. Lu, F. Ciucci, *Chem. Mater.* **2017**, *29*, 9308–9319.
[46] R. Asakura, L. Duchêne, R.-S. Kühnel, A. Remhof, H. Hagemann, C. Battaglia, *ACS Appl. Energy Mater.* **2019**, *2*, 6924–6930.
[47] N. Nitta, F. Wu, J. T. Lee, G. Yushin, *Mater. Today* **2015**, *18*, 252–264.
[48] A. Unemoto, T. Ikeshoji, S. Yasaku, M. Matsuo, V. Stavila, T. J. Udovic, S. Orimo, *Chem. Mater.* **2015**, *27*, 5407–5416.
[49] W. Zhao, R. Zhang, H. Li, Y. Zhang, Y. Wang, C. Wu, Y. Yan, Y. Chen, *ACS Appl. Mater. Interfaces* **2021**, *13*, 31635–31641.
[50] T.-T. Zuo, R. Rueß, R. Pan, F. Walther, M. Rohnke, S. Hori, R. Kanno, D. Schröder, J. Janek, *Nat. Commun.* **2021**, *12*, 6669.
[51] L. M. Riegger, R. Schlem, J. Sann, W. G. Zeier, J. Janek, *Angew. Chem. Int. Ed.* **2021**, *60*, 6718–6723; *Angew. Chem.* **2021**, *133*, 6792–6797.
[52] T. Famprikis, P. Canepa, J. A. Dawson, M. S. Islam, C. Masquelier, *Nat. Mater.* **2019**, *18*, 1278–1291.
[53] J. Auvergniot, A. Cassel, J.-B. Ledeuil, V. Viallet, V. Seznec, R. Dedryvère, *Chem. Mater.* **2017**, *29*, 3883–3890.
[54] F. Walther, R. Koerver, T. Fuchs, S. Ohno, J. Sann, M. Rohnke, W. G. Zeier, J. Janek, *Chem. Mater.* **2019**, *31*, 3745–3755.
[55] R. Koerver, I. Aygün, T. Leichtweiß, C. Dietrich, W. Zhang, J. O. Binder, P. Hartmann, W. G. Zeier, J. Janek, *Chem. Mater.* **2017**, *29*, 5574–5582.
[56] Y. Lee, J. Jeong, H. J. Lee, M. Kim, D. Han, H. Kim, J. M. Yuk, K.-W. Nam, K. Y. Chung, H.-G. Jung, S. Yu, *ACS Energy Lett.* **2022**, *7*, 171–179.
[57] Deposition Number 2155436 contains the supplementary crystallographic data for this paper. These data are provided free of charge by the joint Cambridge Crystallographic Data Centre and Fachinformationszentrum Karlsruhe Access Structures service.

Manuscript received: March 7, 2022
Accepted manuscript online: June 4, 2022
Version of record online: June 21, 2022